Hematite nanostructures: An old material for a new story. Simultaneous photoelectrochemical oxidation of benzylamine and hydrogen production through Ti doping

Hematite nanostructures: An old material for a new story. Simultaneous photoelectrochemical oxidation of benzylamine and hydrogen production through Ti doping

Raffaello Mazzaro[a,**], Sara Boscolo Bibi[a], Mirco Natali[b], Giacomo Bergamini[c], Vittorio Morandi[d], Paola Ceroni[c], Alberto Vomiero[a,e,*]

[a] Division of Materials Science, Department of Engineering Science and Mathematics, Luleå University of Technology, 971 87 Luleå, Sweden
[b] Department of Chemical and Pharmaceutical Sciences, University of Ferrara, Via L. Borsari 46, 44121 Ferrara, Italy
[c] Chemistry Department "Giacomo Ciamician , University of Bologna, 40129 Bologna, Italy
[d] CNR-IMM Bologna, Via Piero Gobetti 101, 40139, Bologna, Italy
[e] Department of Molecular Sciences and Nanosystems, Ca Foscari University of Venice, Via Torino 155, 30172 Venezia Mestre, Italy

Keywords:
Hematite
Photoelectrochemistry
Photoanode
Benzylamine
Hydrogen

A B S T R A C T

Overall water splitting represents one of the most promising approaches toward solar energy conversion and storage, which is, however, severely challenged by the four-electron/four-proton nature of the oxygen evolution reaction (OER). One option to overcome this issue is to replace OER with a more useful reaction, for simultaneous production of both hydrogen and chemicals of interest. For the purpose, in this paper a cheap, hydrothermally prepared Ti-doped nanostructured hematite photoanode was employed for the f rst time as highly stable, heterogeneous catalyst for the low bias, efficient and highly selective photoinduced oxidation of benzylamine to N-benzylidenebenzylamine, and for the simultaneous production of hydrogen in a double solvent/environment cell. A preliminary estimate indicates the possibility to obtain a ~150 μmol h^{-1} H_2 production, with the contemporary production of stoichiometric benzylidene N-benzylamine in a 5 × 5 cm^2 area electrode. This study contributes to overcome the 40-year lasting issues limiting the use of hematite in industrial photoelectrochemical sunlight conversion and storage, due to poor performance of hematite and lack of economic value of oxygen production, providing solid evidence for the use of hematite in alternative oxidation reactions of industrial importance.

1. Introduction

The energy from the sun is one of the most appealing sources of clean and renewable energy, being only 80 min of solar irradiation on Earth's surface enough for the fulfilment of approximately all the human energy demand for one year [1]. Despite the exciting premises, solar energy is extremely distributed and intermittent, therefore its exploitation hinges on the efficient storage into more reliable forms, such as electricity or chemical energy. While photovoltaic devices are nowadays largely employed, the energy produced by them should be used immediately or stored in secondary accumulation devices. An alternative and smart approach to avoid this further step consists in storing the energy captured from sunlight within chemical bonds, such as H_2 or CO_2 byproducts [2]. In particular, water splitting, i.e. the production of H_2 and O_2 from water through hydrogen and oxygen evolution reactions (HER and OER), represents a clean reaction with a thermodynamic potential as low as 1.23 eV, far lower than the energy of all the photon in the visible spectrum [3]. Despite that, the practical implementation of water splitting is a challenge that is still far from being overcome, and the main reason lies in the four-electron/four-proton nature of the OER, resulting in a substantially large overpotential for achieving sufficient water splitting efficiency.

Interestingly, the OER product, i.e. oxygen, is not particularly valuable from the industrial point of view, at least considering its high content in the atmosphere. A possible solution to this unresolved issue might be to replace the OER with a less challenging and more useful reaction, towards the simultaneous production of hydrogen and valuable chemicals [4]. Many different oxidation reactions might fulfil the requirements to this aim, such as the oxidation of alcohols to aldehydes and ketones [5 8], amines to imines [9,10] as well as cross-coupling

* Corresponding author. Division of Materials Science, Department of Engineering Science and Mathematics, Luleå University of Technology, 971 87 Luleå, Sweden
** Corresponding author.
E-mail addresses: raffaello.mazzaro@ltu.se (R. Mazzaro), alberto.vomiero@ltu.se (A. Vomiero).

reactions [11 13] and biomass derived intermediate compounds [14]. A key factor to succeed in this approach is the choice of the photocatalysts, which absorb the light and convert it to excited holes and electrons that are promoting either the reduction or the oxidation reaction, or both. A large number of organic molecules and metal complexes have been proposed for organic photocatalysis application in a purely homogeneous approach. While these catalysts have been successfully employed for complex reactions [15,16], both in the oxidative and reductive paths, their large-scale employment in industrial devices is limited by the lack of stability and the challenging recovery of the catalyst after the organic reaction. In addition, the typically employed homogenous setup does not allow for the use of different solution environments, whereas the use of supported inorganic heterogeneous catalysts in a photoelectrochemical cell allows for a more flexible experimental setup [17].

Among heterogeneous systems [18,19], the most used inorganic catalyst for oxidative reactions is certainly TiO_2, whose deep valence band allows for high oxidative photo-potential, often exploited for organic pollutants degradation [20]. Despite its stability and optimal catalytic activity, TiO_2 is characterized by a large band gap (~3.2 eV), limiting its employment to UV irradiation. Some efforts have been devoted to broaden its activity in the visible region, for instance through the dye-sensitizing approach [18]. Recently, lower band-gap semiconductors have also been employed, such as $BiVO_4$ [7], Bi_2WO_6 [21] and $PbBiO_2X$ [22] (X = Cl, Br), achieving interesting results. Graphitic C_3N_4 is a promising alternative to these materials due to the lack of toxicity, the low fabrication cost and the highly reducing properties (conduction band at −1.3 V vs NHE, pH 7 [23]). Whereas this material holds some potential [23 25], its use as photocatalyst is still limited by its low absorption coefficient in the visible region, the lack of precise control on the polycondensation synthesis method, as well as the relatively low photo-induced oxidation potential, limiting the application in organic oxidative reactions. Cadmium sulphides and selenides have also been often employed as photocatalyst for hydrogen production [26,27], sometimes coupled to simultaneous oxidation of various alcohols to aldehydes [8,28], but lacking of sufficient stability for practical application.

α-Fe_2O_3, i.e. hematite, is traditionally one of the most applied and promising materials for water oxidation since its first proposal by Bard et al., in 1976 [29] being stable, widely available, cheap and environmental friendly. Thanks to the 2.1 2.3 eV band-gap and the n-type character, this material has been often used as a photoanode in photoelectrochemical cells [30]. However, its fairly positive conduction band potential, usually in the +0.2 0.6 V range vs SHE, is preventing the utilization as single photocatalyst for both HER and OER. This has been usually exploited by employing a small positive bias or by coupling the photoanode to a second semiconductor photocathode in a tandem-cell configuration [30]. Hematite is also characterized by some disadvantages when applied to water oxidation and all the other photocatalytic application, such as the poor charge mobility, the short exciton lifetime, the medium light penetration depth (α^{-1} = 118 nm at λ = 550 nm) and very short hole diffusion length (2 4 nm), limiting the photocatalytic performance [30]. Several possible solutions were tried to circumvent these limitations. Nanostructuring the surface of the hematite film increases the surface area and shortens the pathway that photocarriers have to cover to carry out the complete photocatalytic reaction [31]. The inclusion of a hematite compact thin film (buffer layer) between the conducting oxide substrate and the nanostructured hematite film has been reported to direct the growth of hematite nanostructures and positively affect the recombination rate at the substrate/hematite interface [32,33].

On the other hand, the carrier mobility can be enhanced through substitutional doping with several elements, such as Si^{4+} [34], Mn^{4+} [35], Sn^{4+} [36,37] and Ti^{4+}, following the aliovalent doping concept [35]. Ti^{4+} doping has been largely and successfully employed to dope hematite, often coupled to co-catalysts or surface treatments [38], but the role of the Ti^{4+} impurity is still controversial. The improvement of photocatalytic performance has been attributed to i) the increased electron concentration [39], ii) the variation of morphology [40], iii) the suppression of surface state recombination paths due to the Ti^{4+}-induced surface electric field [41] and iv) the formation of mixed oxide phases [42], typically forming an overlayer improving the charge separation and transfer at the semiconductor-electrolyte interface [43].

Despite the recent re-discovery of the field of organic photocatalysis [44], few attempts to use hematite photoanodes as photo-electrocatalysts for organic oxidative reaction has been reported in the literature, basically limited to ethanol and methanol oxidation [45].

In the present paper, we propose an innovative photocatalytic approach for the low-bias photoelectrochemical oxidation of benzylamine and simultaneous proton reduction by applying Ti-doped hematite nanorod photoanodes. The benzylamine main oxidation product, N-benzylidenebenzylamine, is a valuable intermediate in organic synthesis [46] and it is usually synthesized by stoichiometric chemical oxidation [47], therefore the current photocatalytic approach represents a greener and appealing alternative. In addition, by applying a small bias, we investigated the feasibility of performing simultaneous proton reduction to hydrogen at the counter-electrode, through a dual reaction environment configuration (Fig. 1a), allowing for efficient and extremely selective anodic and cathodic reactions.

The electrodes are prepared by extremely cheap, scalable and environmentally friendly hydrothermal method. The photocatalytic properties are correlated with the morphology, composition and structure of the material. In particular, we demonstrated that Ti doping results in increased hole mobility and in the activation of the surface layer. Photoanode optimization boosted its efficiency, achieving photocurrents as high as 1.2 mA cm^{-2} with +0.8 V external bias applied. These results pave the way for the large-scale exploitation of Ti-doped nanostructured hematite as photodetectors for applications with industrial relevance.

2. Results and discussion

2.1. Morphological and structural characterization

Hematite electrodes were hydrothermally grown on FTO glass after deposition of a compact hematite buffer layer (see the experimental section and Fig. 1b). Two different concentration of Ti dopant were added to the growth solution, respectively equal to 1% and 5% with respect to Fe content (atomic %), in addition to a reference, undoped sample.

Fig. 2a displays the cross-sectional SEM micrographs for the produced Fe_2O_3 electrodes. The film is homogeneously deposited on the whole unmasked area. The undoped sample in presence of buffer layer is showing a porous structure composed of vertically aligned nanorods (NRs) sintered together. We infer that this compact morphology is induced by the increased number of nucleation sites provided by the buffer layer with respect to the typical morphology of hydrothermally grown hematite nanorods [37], leading to a denser nanorods array, finally sintered in the compact layer upon thermal annealing. The thickness of this film is equal to (370 ± 60) nm.

The addition of doping impurities in the growth solution is resulting in a dramatic change in morphology, as previously reported [48,49]. Indeed, the addition of 1% or 5% Ti to the growth solution is resulting in an almost complete loss of the ordered quasi-vertical structure, towards a more random deposition of smaller, elongated particles. While in the 1% doped sample, some residual nanorods with reduced length (< 100 nm) can be still recognized, the addition of 5% Ti is resulting in a complete loss of the nanorods morphology towards small, randomly shaped nanoparticles.

While the determination of the thickness of the hematite layer is not completely reliable for such inhomogeneous samples, from a statistical analysis on the SEM micrographs we estimate a thickness ranging from

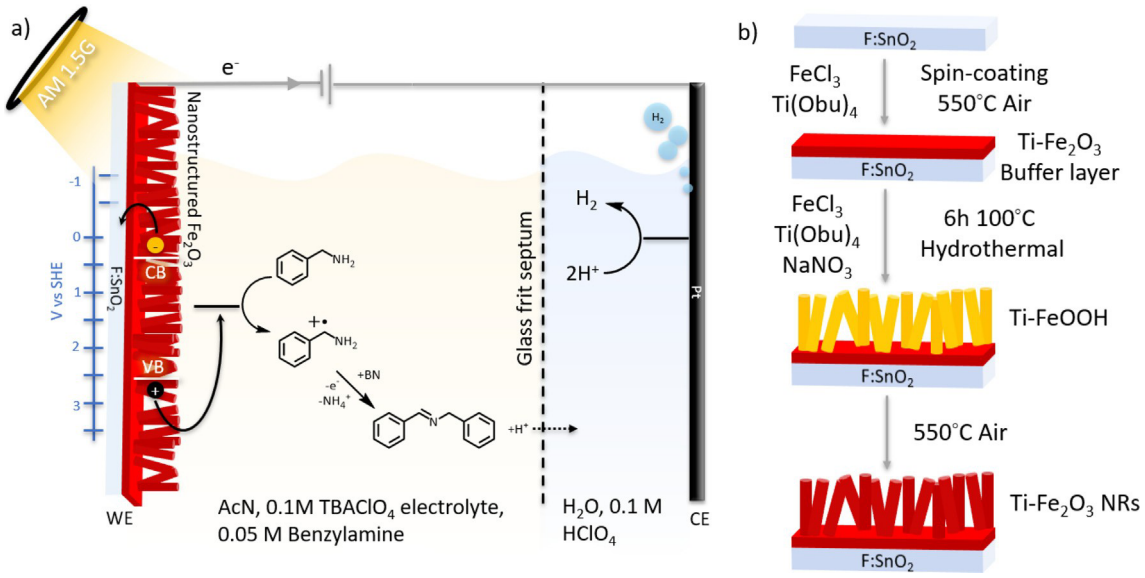

Fig. 1. a) Schematic representation of the proposed photoelectrochemical setup for the simultaneous photo-oxidation of benzylamine and hydrogen production using α-Fe_2O_3 nanostructured photoanodes. b) Synthetic steps for the synthesis of Ti doped hematite photoanodes.

250 to 350 nm, slightly increasing for the 5% doped sample.

The crystal phase of the electrodes has been studied by XRD, using clean FTO glass as reference to remove the contribution of the underlying substrate (Fig. 2b). All the residual peaks, coming from the deposited iron oxide layer, can be indexed to hematite hexagonal phase (JPCSD #33 0664), independently of the amount of Ti or doping. ATR-IR analysis (Fig. S1a) did not display any residual FeOOH phase, consistently to what observed from the XRD patterns. As expected, the relative intensity of the undoped sample is higher with respect to the doped samples, due to the higher thickness and more dense structure. By performing the peak fitting through Rietveld refinement, we can give some insight on the average preferred orientation of the nanorods. For the two most intense peaks, (104) and (110), having 100% and 70% intensity in the reference diffractogram, respectively, we can observe a dramatic difference between the doped and undoped samples. The undoped sample is characterized by the preferential growth along the 110 axis, as demonstrated by the (110)/(104) peak ratio equal to 18.8. On the other hand, the doped samples are showing far smaller values for the same peak ratio, equal to 1.3 and 1, for 1% and 5% doping, respectively, proving that the addition of Ti during the hydrothermal growth is reducing the degree of control on the formation of elongated crystallites, towards a random distribution of spherical nano-particles. Nevertheless, these nanoparticles are formed by single crystals of hematite, as confirmed by HR-TEM analysis (Fig. 2c and d), where no contrast variation is observed due to the formation of heterogeneous interface. The presence of doping Ti is confirmed by Energy Dispersive

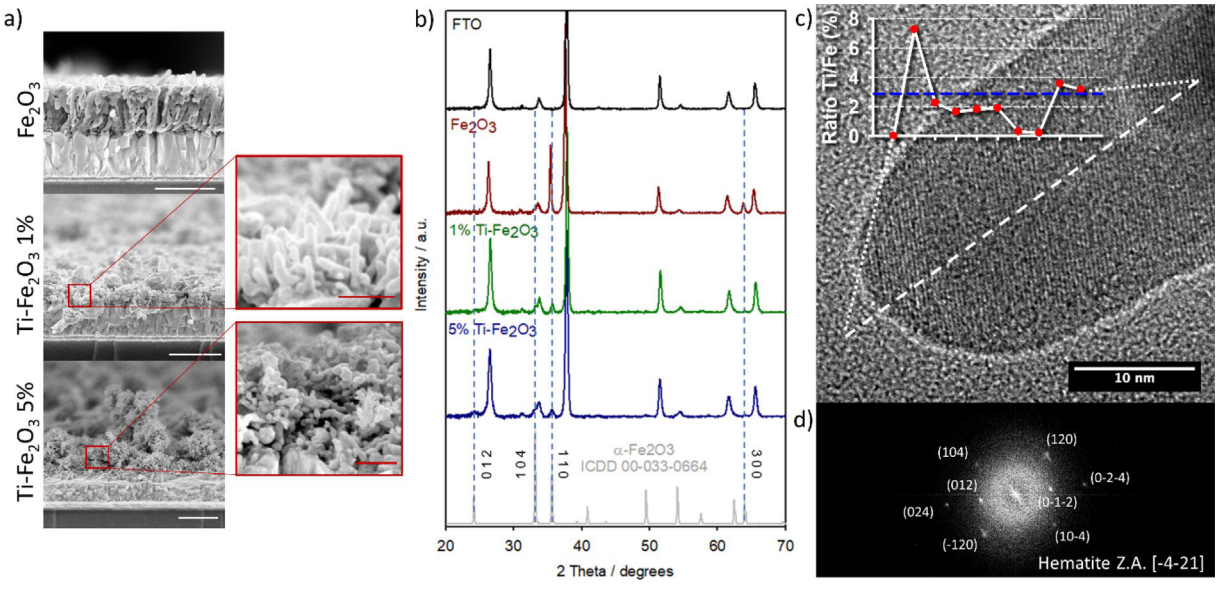

Fig. 2. a) SEM micrographs reporting the cross-section of the hematite photoelectrodes, namely (top) undoped Fe_2O_3, (centre) 1% Ti-doped Fe_2O_3 and (bottom) 5% Ti-doped Fe_2O_3. Scale bar equal to 500 nm. In the inset, higher magnif cation of the doped hematite nanostructures is reported, with scale bar equal to 100 nm. b) XRD patterns of the prepared hematite electrodes at different Ti doping concentrations. The XRD pattern of the FTO substrate and the simulated spectrum for the reference hematite structure (ICDD 00-033-0664) are reported respectively at the top and the bottom of the f gure. The main hematite peaks recognized in the spectra are highlighted with dashed lines reporting the lattice index. c) HR-TEM micrograph of the 1% TieFe_2O_3 sample and d) relative Fast Fourier transform, displaying the ref ection pattern of hematite [-4-21] zone axis. In the inset the EDS prof le extracted by STEM analysis performed on the same nanorod (dashed white line), specif cally displaying the Ti/Fe ratio. The dashed light blue line is displaying the average Ti/Fe ratio, equal to 2.7%.

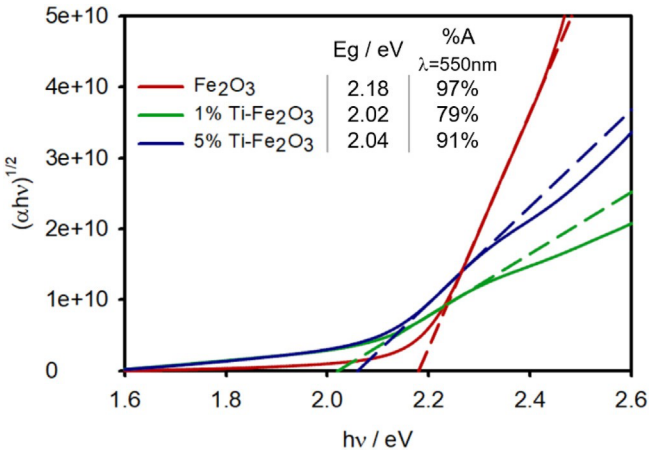

Fig. 3. Tauc plot of the hematite electrodes (continuous lines) and relative linear f tting (dashed lines), whose intercept with the x-axis is equal to the optical band gap (E_g). The coefficient n = 2 has been applied due to the indirect character of the semiconductor transition. In the inset: Optical band gap energies (E_g) calculated by the linear f tting of the Tauc plot, and fraction of photons (%A) absorbed at λ = 550 nm, obtained by the analysis of Transmittance and Diffused ref ectance reported in Fig. S2 and Fig. S3.

X-ray spectra (Fig. S1b). The Ti distribution (Fig. 2c, inset) displays a maximum on the edge of the nanorod, as previously observed [35], and a lower amount within the nanorod, decreasing upon increasing the distance from the nanorod surface, consistent with a Ti doping gradient along the growth axis. It is worth noting that the increase Ti/Fe ratio observed at the end of the EDS line profile is due only to the superposition of the two nanorods shown in the HR-TEM image. While no characterization of the redox state of the Ti dopant is reported here, this has been previously determined multiple times to be +4, resulting in an increased number of oxygen vacancies in the hematite lattice [39 41,43,48,50 53].

2.2. Optical properties

The electrodes display the typical red-orange appearance of hematite thin-films with absorption onset in the 550 580 nm range (Figs. S2 and S3). The band-gap has been determined by fitting the absorption coefficient trends through the Tauc relationship (Fig. 3) as described in the SI, and the resulting values are reported in the inset. The band gap of the pure hematite samples is within the previously reported range for hematite, usually between 2.0 and 2.2 eV depending on the method of preparation. Interestingly, a slight but constant decrease of the band gap is observed in the Ti doped samples. This could be resulting from the introduction of intra-band gap states due to the doping impurity [54] or by the formation of a mixed oxide phase with slightly lower band gap.

The different sample thickness and morphology has a role in the absolute fraction of photons absorbed by the thin, nanostructured film. To quantify that, we calculated the absorption and reflection contribution (details in the SI). The resulting fraction of photons absorbed was compared at λ = 550 nm (inset), i.e. where most of the contribution to the absorption spectrum is due to the absorption of the hematite layer, rather than the reflection and diffusion effects from the substrate. Clearly, the undoped samples are absorbing more than the doped ones, as expected by the higher thickness. Consistently, the fraction of photons absorbed by the 5% Ti-doped sample is higher than that of the 1% one.

2.3. Photo-electrochemical characterization

The photoelectrochemical activity of α-Fe_2O_3 NRs electrodes were investigated with respect to the oxidation of benzylamine (BN) to N-benzylidenebenzylamine (BI) in acetonitrile solution. Fig. 4 reports the linear sweep voltammetry obtained upon illumination with AM 1.5G solar simulator. A strong anodic current is starting at approximately +1.2 V vs SHE for all the hematite electrodes. This feature can be observed even in dark condition while it is absent without added BN (data not reported). Therefore, this current enhancement at +1 V is related to the electrochemical benzylamine oxidation.

Only upon illumination, all the samples show a new anodic process with an onset ranging between +60 mV and +330 mV (± 30 mV, 3 samples average) vs SHE, as displayed in Fig. 4a. The onset potential is slightly shifting towards more positive potentials for the doped samples (Fig. S4), even if the large difference in photocurrent density does not allow for an extremely precise estimation of the onset potential for the undoped sample. The anodic photocurrent is saturating (plateau) upon increasing the applied bias, reaching a maximum current density at ca. +700 mV. This plateau is due to the photo-current generated upon the oxidation of BN, as confirmed by the voltage independent plateau typical for photo-generated carrier limited electrochemical processes [35]. From the comparison of the photocurrent curves, it is clear that the Ti doping is resulting in a dramatic increase of current density up to 10 × in the case of 5% Tie Fe_2O_3 with respect to pristine Fe_2O_3, reaching photocurrent as high as ca. 1 mA cm^{-2}. The relative Ti content is also affecting the performance of the photoelectrode, inducing a

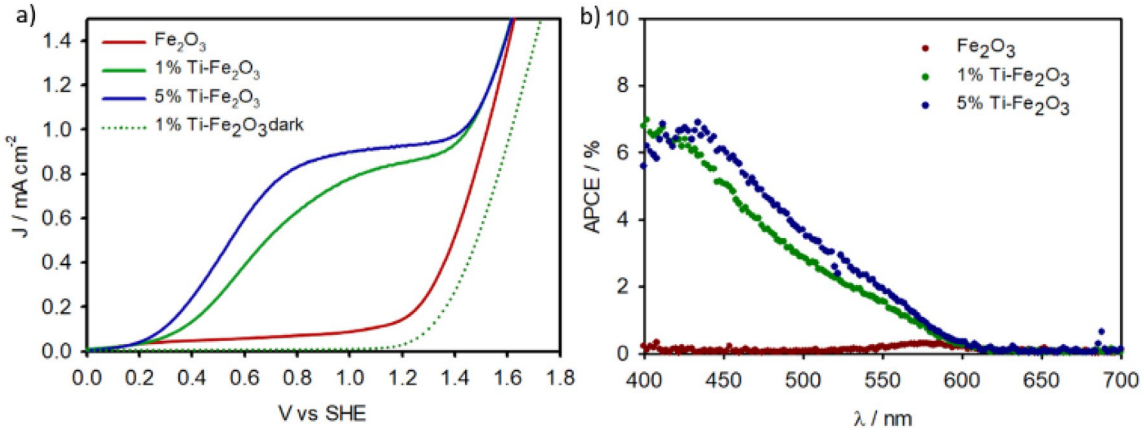

Fig. 4. a) Linear sweep voltammetries of the hematite electrodes in presence of Benzylamine (BN) under AM 1.5G solar simulator illumination. The CV of the 1% Ti doped hematite electrode in dark condition (dashed curve) has also been reported as reference to better visualize the photocurrent produced by the photocatalytic process. b) APCE of the photoelectrodes measured at +0.7 V vs OCV. Measurements were performed in acetonitrile solution of 0.05 M BN and 0.1 M tetrabutylammonium hexaf uorophosphate ($TBAPF_6$).

~10% increase of the photocurrent upon increasing it from 1% to 5%, together with an increase in photocurrent plateau width.

A small photocurrent drop can be observed by performing the same photoelectrochemical experiments with hematite photoelectrodes prepared without buffer layer, as displayed in Fig. S5. The insertion of the compact buffer layer is therefore resulting in slightly better photoelectrochemical performance, as expected, demonstrating that the recombination at the FTO-hematite interface [33] is affecting the photoelectrochemical performance to a small extent. Nevertheless, the different growth kinetics of the hematite layer in presence/absence of buffer layer is resulting in different nanostructure, thus some part of this enhancement might be related to the different morphology.

The Absorbed Photon to Current Efficiency (APCE) of the photoelectrodes (Fig. 4b), measured in the same experimental conditions of the photoelectrochemical experiments, remarks the superior properties of the doped electrodes, with respect to the undoped one. The APCE onset falls approximately at 580 nm for all samples, consistent with the band gap energy extracted from Tauc analysis, proving the light harvesting efficiency of the photocatalyst in the visible light range. Again, a slight enhancement is observed in the 5% sample. The shape of the curve mirrors the one of the transmittance spectra (Fig. S2). The small signal observed for the undoped sample at 550 nm is reasonably due to the collection of the few photoinduced carriers, generated close to the FTO substrate, while at smaller wavelengths holes recombine before being collected, due to both the reduced light penetration (which induces holes generation far from FTO) and the low hole diffusion length. The large difference in APCE between the doped and undoped samples highlights the improved photoelectrochemical performance of the doped sample due to reduced recombination processes.

2.4. Faradaic efficiency and hydrogen evolution

In order to get insight into the chemical transformation of BN during the photocatalytic process we performed a chronoamperometry measurement at +1 V vs SHE over 12 h of continuous irradiation. The product of the reaction has been characterized by NMR (Fig. S6) and the relative yield has been calculated as described in the SI. The results of the chronoamperometry experiment performed on the 5% doped sample (Fig. S7) has been reported in Table 1. We also calculated the faradaic efficiency, defined as the ratio between the product amount and the charge passed through the photoelectrode, divided by the stoichiometric ratio between product and reactants (2 in this case). Even if the faradaic efficiency after 1 h is only about 80%, the value is increasing to almost unitary values with increasing the reaction time to 4 h, reaching a total conversion of about 64% after 12 h. The lower initial faradaic efficiency could be related to some parasitic electrochemical processes due to the presence of low amounts of oxidizable contaminations, such as water, whose contribution becomes negligible over time.

While the product of the oxidative reaction can be characterized by the synergy of electrochemical and NMR spectroscopy, the photochemical reaction induced at the counter electrode is mostly unknown in the single-cell electrochemical experiment. Since the reaction is conducted in aerated environment, we might expect that oxygen is reduced at the counter electrode during the chronoamperometric experiment, where the resulting superoxide ion has been often identified as crucial for the aerobic oxidation of benzylamine [55,56]. The other option involves a back-reduction of the oxidized benzylamine to the starting reagent. Even if the high faradaic efficiency suggests that the latter option is unlikely, we performed a control experiment by insulating the counter-electrode in separated chamber, communicating with the reaction solution through a porous glass-frit. By adding a sacrificial electron acceptor ($AgNO_3$), we could observe a slight increase in the photocurrent registered at the working electrode (SI, Fig. S8), and the faradaic efficiency of the oxidation reaction to benzylamine was calculated to be > 95% also in this case. This is suggesting that the superoxide ion is not involved in the N-benzylidenebenzylamine production, therefore the anaerobic oxidation mechanism discussed by Di Meglio et al. [57] is more compatible to our system, as schematized in Fig. 1a. In addition, this experiment proves that a reduction reaction can be efficiently performed at the counter-electrode without affecting the oxidation of BN to N-benzylidenebenzylamine.

As a consequence, we investigated the possibility of coupling the hydrogen evolution reaction (HER) at the counter-electrode by separating it in an aqueous acidic phase, following the configuration previously schematized in Fig. 1a. The resulting CV is reported in Fig. S9, where only a slight variation of the photocurrent onset potential can be noticed due to the presence of the liquid junction potential [58], with respect to the single environment experiment. The electrolyte ($TBAPF_6$) has been replaced with tetraethylammonium perchlorate to minimize this potential drop across the glass frit junction. Perchloric acid was used to ensure acidic environment in the aqueous phase, as well as good mobility across the junction due to the electrolyte affinity [58]. Due to the interest in both the electrodes activity, a two electrodes config- uration was employed and the chronoamperometry experiment was accompanied by gas chromatography analysis to investigate the amount of hydrogen produced during the photocatalysis experiment. As re- ported in Fig. S9, a slight shift of about +0.3 V of the onset potential for BN photo-oxidation is observed upon switching to the two electrodes configuration. In order to compare the reaction rate with the one of the BN oxidation experiment, a fixed bias equal to +1.3 V was applied during the chronoamperometry experiment, corresponding to +1 V vs SHE. Fig. 5 reports the theoretical amount of H_2 and N-benzylidenebenzylamine (BI) extracted from chronoamperometric experiment by applying the Faraday's law to the integrated charge passing through the electrode. In addition, the experimentally measured amount of products is reported, determined by either GC (H_2) or H NMR (BI). The close

Table 1
Main parameters extracted from the chronoamperometry experiment performed on the 5% $TieFe_2O_3$ sample. The relative BN oxidation to N-benzylidenebenzylamine (BI) yield has been calculated as explained in the SI and reported in the table.

t [h]	Q [C]	n_{e^-} [μmol]	Theoretical conversion [%]	Φ_{NMR}	Faradaic efficiency [%]
1	5.04	52	10.5	8.5	81
2	9.37	97	19.4	17.5	90
4	15.69	162	32.5	33	> 95
12	30.86	319	64.0	62.5	> 95

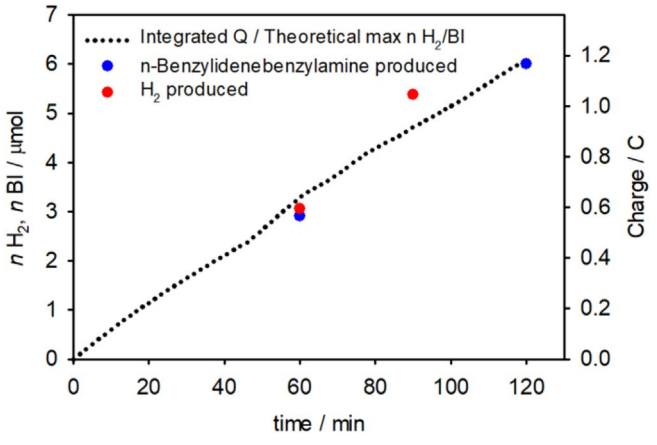

Fig. 5. Theoretical amount (black spotted curve) of H_2 and n-Benzylidene benzylamine (BI) extracted from chronoamperometric experiment performed by applying +1.3 V of external bias, electrode area 0.6 cm^2. In the graph, the experimentally measured amount of H_2 and BI are also reported, determined respectively by GC and H NMR.

match between the calculated and the measured H_2 and BI produced are confirming almost unitary faradaic efficiency for both the HER and the oxidation of benzylamine highlighting the optimal selectivity of the system towards the described photocatalytic cycle. It must be noted that, while the reaction environment for the cathodic reaction is purged with N_2, the anodic reaction takes place in aerobic environment, therefore the presence of oxygen is not affecting the selectivity of the catalyst towards N-benzylidenebenzylamine production.

From this experiment we can calculate an amount of hydrogen produced per unit area equal to 6 1 μmol h^{-1} cm^{-2}, therefore, with proper experimental arrangements, we can calculate that, increasing the electrode area to 5 × 5 cm will result in a ~150 μmol h^{-1} H_2 produced. For comparison purposes, previous attempts of photocatalytic oxidation of organic substrates and simultaneous HER were achieving H_2 production rates ranging from 2 to ~65 μmol h^{-1} [4] It must be noted that these values are achieved in a single-phase, microheterogeneous setup with no addition of external bias, which is certainly overestimating the efficiency of our hematite photoanode. Nevertheless, by simply normalizing the H_2 production ratio for the photocurrent density at different potentials in the 5 × 5 cm example, we can calculate an impressive 60 μmol h^{-1} value with an external overall bias as low as +0.8 V.

In addition, by comparing the initial linear sweep voltammetry of the photoelectrode with the one obtained after the chronoamperometry experiment (Fig. S10), only negligible variation of the photoelectrode behaviour can be observed, proving the excellent stability of the electrode.

2.5. The role of Ti doping

The esults of the photoelectrochemical characterization h ghlights that Ti doping in the hematite structure is strongly activating the hematite photocatalyst, and the activity is directly proportional to the doping impu ity content. As stated in the introduction, there can be several reasons behind this enhancement, and an accurate electrochemical analysis has to be performed to understand them.

A possible reason for the high cathodic current might be the higher surface area of the Fe_2O_3 electrodes thanks to the variation of the nanoscale morphology. Nitrogen physical adsorption-desorption calculations were employed to have an insight on the relative surface area of the samples (Fig S11) Brunauer Emmett Teller (BET) showed a slight drop in surface area on the doped samples, from 1.43 ± 0.42 m^2 g^{-1} of the undoped samples to 0.99 ± 0 50 and 0.93 ± 0.34 m^2 g^{-1} for the 1% and 5% Ti doped samples, respectively. Due to the limited mass loading of the sample, only a qualitative comparison of the relative value can be performed Since the thickness of the samples is also affected by the Ti content, we calculated the BET surface area per geometrical area unit as described in the SI The resulting ratio is equal to 989, 495 and 666 for the pristine, the 1% and the 5% Ti doped samples, respectively. We can therefore confirm that the undoped photoanode is characterized by the largest surface area, whereas the doped samples are both characterized by a strong drop as expected by the loss of the controlled structure observed in the doped samples. Thus, the photocurrent enhancement is clearly not related to the physical surface area.

The electrochemical activity of the surface might be strongly influenced by the Ti addition. As previously observed by Zandi et al. [43], doping hematite with Ti produces a larger number of available surface states to trap holes, by activating the so-ca led “dead layer”. These surface effects can be responsible for both charge transfer rate enhancement and suppress surface recombination, similar to what observed in oxygen evolution catalysts on hematite photoanodes [59]. In order to understand the role of the morphology on the electrochemical activity, we calculated the electrochemical double layer capacitance (C_{DL}) of the semiconductor surface, by measuring the non faradaic capacitive current associated with double-layer charging from the scan-rate dependence of linear sweep voltammograms, as previously reported [60]. The experimental procedure is described thoroughly in the SI, and it is typically resulting in an increasing charging current by increasing the scanning rate, as shown in Fig. S12a. The double layer capacitance can be simply extrapolated from the slope of the linear dependence of the plateau current density against the scan rate (Fig. S12b).

As expected, the C_{DL} observed for the Ti-doped samples is always higher than the one of the undoped samples (Table S1), consistent with a larger number of active sites for benzylamine oxidation

Consistently, the charge transfer resistance at the interface semiconductor-electrolyte is strongly reduced on the doped samples, as displayed by electrochemical impedance spectrosocopy (EIS) analysis The Nyquist plot registered in the faradaic region under illumination (Fig. 6a) is clearly displaying smaller semicircles for the doped samples, with only small variation upon increasing the Ti content, confirmed by the R_{CT} val es calculated by fitting with equivalent circuit (modified Randles circuit, in the inset). With respect to Randles circuit, the capacitance element was replaced with a constant phase element to take into account the distribution of time constants generated by the nanoporous surface [61] and properly fit the experimental data.

A second possible reason for the enhancement of the photoelec trochemical activity might be related to the valence band edge position, determining the potential of the photogenerated holes, as well as the density of majority carriers, responsible for the bulk resistance of the material. Fig. 6b is reporting the Mott-Schottky plots for all the samples in dark conditions, exhibiting positive slope as expected fo n-type semiconductors The linear fit of the sigmoidal function (transition region) with the Mott-Schottky relationship, allows for the calculation of the relative position of the flat band potential (E_{FB})) and the dopant density (N_D) can be determined:

$$\left(\frac{A_s}{C_{sc}}\right)^2 = \frac{2}{q\kappa\varepsilon_0 N_D}\left(V - E_{FB} - \frac{k_B T}{q}\right) \quad (1)$$

where V is the applied voltage, C_{sc} is the space charge capacitance A_{SC} is the surface area (geometrical area used in this case due to a lack of absolute method for the active surface area), k_B is the Boltzmann's constant, T is the absolute temperature, q is the elementary charge, κ is the dielectric constant of the semiconductor (32 for the hematite) [62] and ε_0 is the vacuum permittivity ($8\,854 \times 10^{-12}$ C V^{-1} m^{-1})

Table 2 is resuming the E_{FB} and N_D esulting from the fitting of the curves in Fig. 6b, as well as the same values obtained upon illumination with AM 1.5G light (Fig. S14). As a first observation, we can notice that the doped samples are displaying more positive E_{FB} in the dark with respect to the undoped samples, as previously reported for Ti-doped hematite [53] The flat band potential for the undoped is rather negative with respect to the one usually reported for hematite, between +0.4 and + 0 6 V vs SHE [41,63,64], but the different solution environment, thus the different donor density [65], should be considered in the evaluation of the measured potential. The valence band edge potential (E_{VB}) can be therefore estimated from the optical band gap (E_g) value of about +2 3 V for the undoped sample, and +2 60 2 70 V vs SHE for the 1% and 5% Ti-doped samples. Despite the E_{VB} absolute value is only approximate, also in light of the recent studies on the nature of polaron states in doped hematite [66] and the consequences on the position of E_{VB} and E_{CB}, the relative value can be compared among the prepared samples. Therefo e, the potential of the photo generated holes is expected to be higher in the Ti doped samples, promoting the photo-oxidation process.

Upon illumination, we can observe a ΔE_{FB} towards more positive potentials of about +100 mV and + 80 mV for the 1% and 5% Ti-doped samples, while only a slight variation (+25 mV) was observed for the undoped sample. This behaviour was previously identified as related to the surface-states charging in hematite thin films, whose magnitude is related to the amount of surface charges [64]. The higher magnitude of ΔE_{FB} for the doped samples can be related to the higher

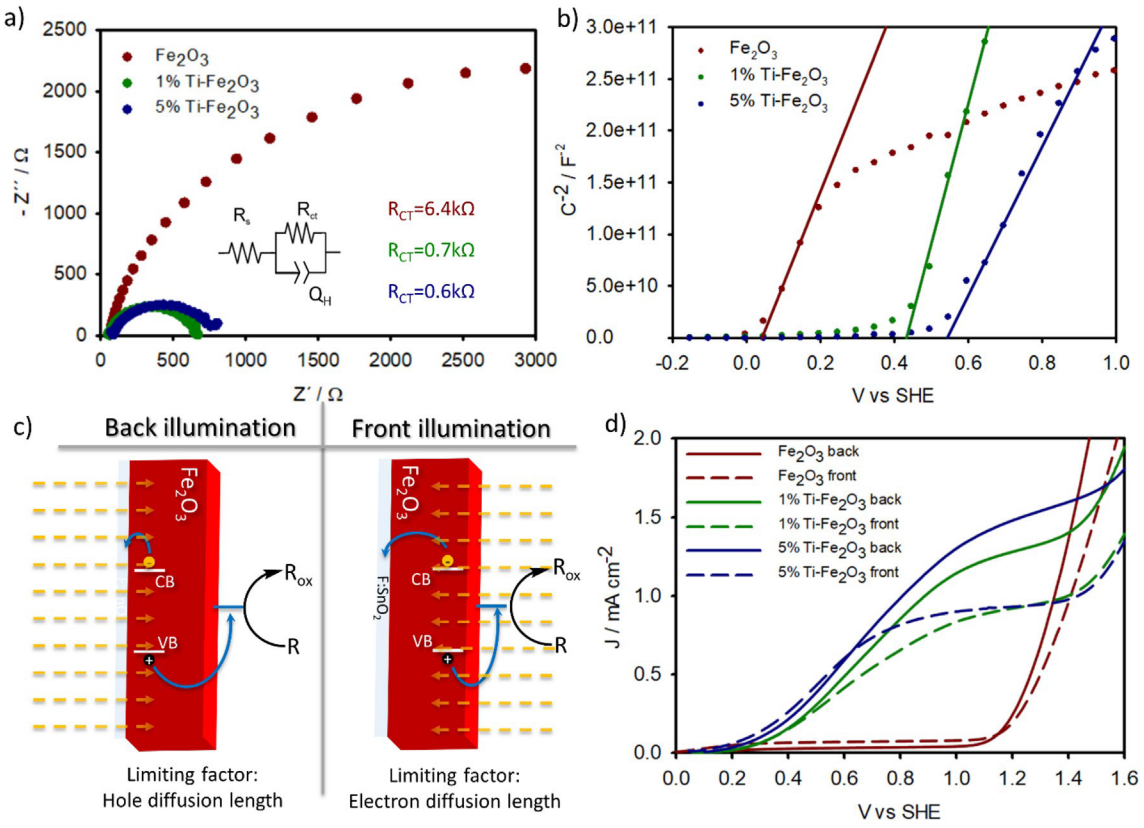

Fig. 6. a) Potentiostatic EIS experiment at 1 V vs SHE upon illumination with AM 1.5G f ltered solar simulator. b) Mott-Shottky plots of the prepared electrodes in dark conditions in presence of BN (spotted lines) obtained from impedance spectra (see Supporting Info discussion). The linear f tting used to calculate the f at band potential (E_{FB}) and the donor density (N_D) through the Mott-Schottky equation is also reported (straight solid lines). c) Schematic representation and d) experimental curves obtained from a linear sweep DC voltammetry experiment under AM 1.5G solar simulator illumination either from the semiconductor-electrolyte side (front) or the semiconductor-substrate side (back). Measurements performed in acetonitrile solution of 0.05 M BN and 0.1 M $TBAPF_6$.

number of surface sites previously assessed by the double layer capacitance.

Opposite to the E_{FB}, N_D values are not strongly affected by the Ti content, with a slight increase in the 5% sample only. The absolute values of the undoped samples are higher than the ones reported previously for hematite [67], but no correction for the real surface area was applied due to: (i) the lack of reliability of the BET surface area measurement in this mass loading range; (ii) the impossibility to obtain a precise value for the electrochemically active surface area due to the lack of specific capacitance in this solution environment to compare with the obtained double layer capacitance. Therefore, we expect a systematic overestimation of the present values, while the real values should be lower, when taking into account the nanostructured surface, and more consistent with the literature. In addition, the different nanoscale morphology might affect the space charge layer, proportionally underestimating the donor concentration with the decreasing size of the nanomaterial domains [62]. Nevertheless, the lack of N_D improvement upon addition of Ti points out that the observed photoelectrochemical enhancement is not due to an increase of majority carriers (electrons).

Interestingly, upon illumination of the semiconductor with AM 1.5 G source, all samples undergo a slight increase of N_D, slightly higher in the doped samples. This could be related to the higher mobility of the photogenerated charges in the doped samples with respect to the undoped ones [68].

To confirm this hypothesis, a comparison between the photo-electrochemical J-V curves was performed, by illuminating the sample either from the electrolyte or the glass side of the nanostructured film (Fig. 6c). Indeed, due to the low charge diffusion length and light penetration depth (α^{-1} = 118 nm at λ = 550 nm), the illumination side has been observed to affect the photocurrent behaviour of hematite photoelectrodes [69].

Indeed, due to the limited light penetration depth, the depletion layer is mainly localized at the semiconductor-electrolyte junction, in the front illumination setup, therefore the current is limited by the electron diffusion length across the semiconductor. On the opposite, by illuminating the sample on the semiconductor-FTO interface, the photogenerated electrons are efficiently collected by the conductive oxide, while the holes must diffuse across the hematite layer to reach the surface-electrolyte interface.

The undoped sample exhibits a large drop in photocurrent in the back-illumination configuration with respect to the front configuration (Fig. 6d), due to the inefficient hole transport across the semiconductor, unable to reach the semiconductor-electrolyte interface. Thus, the hole diffusion length is certainly a predominant limiting factor in the

Table 2
Main results of the Mott-Schottky analysis for the prepared hematite electrodes.

Composition	E_{FB} dark [V vs SHE]	N_D dark [10^{19} cm^{-3}]	E_{FB} light [V vs SHE]	N_D light [10^{19} cm^{-3}]
Fe_2O_3	0.070	1.97	0.094	2.18
1% Ti-doped Fe_2O_3	0.458	1.31	0.552	3.11
5% Ti-doped Fe_2O_3	0.569	2.45	0.745	2.98

undoped sample.

On the other hand, the doped samples are exhibiting a moderate photocurrent enhancement upon illuminating the sample from the glass side, about ~20% and ~30% for the 1% and 5% Ti doped samples, respectively, suggesting that one of the limiting factors for the low APCE in the doped sample lies in the limited photogenerated electrons diffusion length. The opposite behaviour, with respect to the undoped sample, suggests also that the hole diffusion length is no more a limiting factor. This is likely due to higher intrinsic hole diffusion length, but the smaller crystal domains, highlighted by the SEM micrographs, can also play a role.

Nevertheless, whereas the superior properties of Ti doped hematite is often explained with the increased donor density resulting from the substitutional doping, a combination of modified morphology, increased hole diffusion length and surface effects is more likely to explain the photocurrent enhancement in our samples.

3. Conclusion

We demonstrated the possibility to apply Ti-doped hematite photoanodes for the efficient and selective photoinduced oxidation of benzylamine to N-benzylidenebenzylamine, and for the simultaneous production of hydrogen in a double solvent/double environment cell, by applying external bias as low as +0.6 V and employing a conventional Pt counter electrode. The morphology and the doping with Ti impurities are critical to boost the photocatalytic activity of the nanostructures. Doping with 1% 5% of Ti allows to dramatically increase the photocatalytic performance of hematite, achieving high photocurrents upon illumination with visible light. The source of the increased efficiency has been identified as a combination of the increased holes mobility and the activation of the surface layer. Both the oxidation of the organic substrate and the production of hydrogen are displaying almost unitary faradaic efficiency, proving the selectivity of the photocatalyst. With proper experimental arrangements, we can estimate that, by increasing the electrode area to 5 × 5 cm^2, a ~150 μmol h^{-1} H_2 production rate can be achieved, with the contemporary production of stoichiometric N-benzylidenebenzylamine. The use of extremely cheap and widely available materials like hematite is of the utmost importance for the industrial application. In addition, the use of the hydrothermal growth technique allows for easy and affordable scale-up, as well as large flexibility with respect to the use of different substrates sizes and materials. In the past, the economic value provided by the photoelectrochemical water splitting reaction has proved to be hardly affordable for large-scale application due to the poor performance of hematite photoanodes and the lack of economic value of the oxidation process. This study provides a solid proof of principle for the use of hematite photoanodes in alternative oxidation reaction, whose increased product added value might allow for feasible implementation of industrial scale photoreactors.

4. Experimental section

Fe_2O_3 buffer layer deposition. The Fe_2O_3 buffer layer was prepared by spin-coating followed by annealing in air [33]. Fluorine-doped tin oxide (FTO) coated glass slides (2.5 × 1.5 cm, Pilkington TEC8, 8 Ohm/sq. sheet resistance) were accurately cleaned through ultrasonication and rinsing steps (deionized water (DW), acetone, ethanol). 1 cm^2 of the slide was masked to allow for direct contact on FTO during the electrochemical experiments. A 0.15 M solution of ferric chloride in 2-butoxyethanol was prepared, and titanium butoxide ($Ti(OBu)_4$) was added to the solution (5% with respect to iron content) as Ti source. No precipitation occurs during the addition. 70 μl of the solution was deposited on the FTO slide, followed by spin coating (10 s at 1000 RPM, then 30 s at 3000 RPM). The procedure was repeated 3 times to increase the thickness of the film and allow for homogenous deposition. The slides are finally annealed at 500 °C for 1 h.

Fe_2O_3 electrodes growth. The Fe_2O_3 nanostructured electrodes were prepared by slightly adapting a previously reported method [50]. Typically, a 0.15 M ferric chloride ($FeCl_3{\cdot}6H_2O$) and 1 M sodium nitrate ($NaNO_3$) in DW was prepared. Again $Ti(OBu)_4$ was rapidly added to the solution as Ti source, with two different concentration ratios (1% and 5% vs Fe). The solution was stirred for 10 min to allow for partial dissolution of the hydrolysed $Ti(OBu)_4$. The pH of the solution was adjusted to 1.5 with HCl. FTO glass slides were suspended horizontally in a homemade Teflon-lined stainless-steel reactor thanks to a specifically made PTFE support, with the conductive side facing down. Typically, the synthesis was simultaneously performed on pristine FTO glass slides, and buffer layered covered ones. The reactor is closed and placed in an oven at 100 °C for 6 h. The produced electrodes are then thoroughly rinsed with DW and annealed at 500 °C for 2 h. Control experiments were performed without the addition of the Ti source, to investigate the doping effect on the morphological and functional properties.

Morphological, structural and optical characterization. Scanning electron microscopy (SEM) cross-section images were collected on a FEI Magellan 400 HR-SEM. High resolution transmission electron microscopy (HR-TEM) and scanning transmission electron microscopy (STEM-HAADF) characterization was performed on a FEI Tecnai F20 equipped with a Schottky emitter operating at 200 kV. The chemical composition was verified by means of energy dispersive spectrometry (EDS) by using an EDAX Phoenix spectrometer equipped with an ultrathin window detector. X-ray diffraction (XRD) pattern were registered on a PanAnalytical Empyrean XRD in reflection mode, equipped with monochromator to minimize Fe luminescence. Nitrogen ad- sorption desorption isotherms and the Brunauer Emmett Teller (BET) surface areas were determined with a Micromeritics ASAP2010 station operated at 77 K. The sample was degassed at 473 K overnight and then analysed at 77 K. The relative pressure (P/Po) range used for calculation of BET surface area was from 0.05 to 0.35. The thin film samples were weighed before analysis and a clean FTO slide was used as reference. Transmittance and Diffused Reflectance characterization was performed on an Agilent CaryUV 5000 double beam spectrophotometer equipped with integrating sphere.

Photo-electrochemical experiments. The electrodes were placed in a glass cylindrical cell (Bio-logic) filled with 6 mL of a 0.1 M solution of N-Tetrabutylammonium Hexafluorophosphate in Acetonitrile (anhydrous) ($TBAPF_6$). Unless stated otherwise, Pt wire and $Ag/AgNO_3$ (0.01 M $AgNO_3$ in 0.1 M $TBAPF_6$ in Acetonitrile) electrodes were used as counter and reference electrodes, respectively. AM1.5G Solar Simulator was used as light source, tuning the power output to 100 mW cm^{-2} with a calibrated photovoltaic (PV) cell. The photoelectrodes are dipped into the electrolyte solution with the deposited hematite thin film facing the light source, carefully regulating the immersed area to 1 cm^2. Voltammetry experiments were performed in diffusion-limited conditions, whereas long time chrono-amperometry experiments (4 12 h) were carried out gently stirring with a magnetic stirrer. A Solartron Analytical ModulabXM electrochemical station was employed for all the electrochemical characterization.

Spectral responsivity. Incident Photon to Current Efficiency (IPCE) experiments have been performed in the same experimental conditions as the photoelectrochemical experiments. The potential was set to +1.2 V vs SHE. Absorbed Photon to Current efficiency was calculated by dividing IPCE for the fraction of photon absorbed at each wavelength, calculated as described in SI.

Nuclear magnetic resonance (NMR) characterization. The products of benzylamine oxidation were characterized by ^1H NMR after several purification steps [57]. The reaction solution was first washed with 15 20 mL of diethyl ether to precipitate the electrolyte, then filtered over 0.22 μm PTFE syringe filter and vacuum dried. The organic yellow oil was dispersed in $CDCl_3$ for NMR characterization. H NMR spectra were collected by a Varian MR 400 MHz NMR.

H_2 photoelectrochemical production experiments. The hydrogen

evolution experiments were carried out upon solar-simulated irradiation of a custom-made gas-tight reactor composed of two compartments separated by a frit. The first compartment, containing the BN in acetonitrile, has two ports which are used for the working and the reference electrodes, respectively. A hematite photoelectrode (working electrode) with only 0.6 cm^2 surface area was used and connected to a copper wire (sealed inside a glass stick) using copper tape, a saturated calomel electrode (SCE, *Amel*) was used as a reference to calibrate for the potential variation. The second compartment, containing the acidic aqueous solution, has two ports as well, one is used for the platinum counter electrode and the second one is connected to a closed headspace from which automatic withdrawal by the GC pump takes place for gas detection and quantification. All connections involving electrodes are gas-tight (*Ace Glass Inc., USA*). The gas atmosphere of the first compartment is analysed on an *Agilent Technologies 490 micro-GC* equipped with a 5 Å molecular sieve column (10 m) and a thermal conductivity detector. Argon was used as the carrier gas. 5 mL from the headspace are sampled by the internal GC pump and 200 nL are injected in the column maintained at 60 °C for separation and detection of gases. The unused gas sample is then reintroduced in the reactor in order to minimize its consumption along the whole experiment. The amount of hydrogen produced during the photo-electrolysis was quantified from a calibration procedure based on a galvanostatic electrolysis (−0.5 mA, 1 h) of a 0.1 M H_2SO_4 solution with a Pt electrode using the same setup and experimental conditions. A 100% faradaic efficiency was assumed leading to a linear correlation between the amount of hydrogen evolved at the Pt cathode and the electrolysis time.

Acknowledgements

R.M. and A.V. acknowledge the Knut & Alice Wallenberg Foundation and the Kempe Foundation for the financial support. A.V. acknowledges the European Union's Horizon 2020 research and innovation programme under grant agreement No 654002 for partial financial support. A.V. acknowledges the Olle Engkvists Byggmästare Foundation for the financial support. We want to thank G. Valenti and F. Paolucci for the useful discussion about electrochemical analysis.

References

[1] M. Grätzel, Photoelectrochemical cells, Nature 414 (2001) 338–344, https://doi.org/10.1038/35104607.
[2] J. Wu, Y. Huang, W. Ye, Y. Li, CO2Reduction: from the electrochemical to photochemical approach, Adv. Sci. 4 (2017) 1–29, https://doi.org/10.1002/advs.201700194.
[3] V. Balzani, L. Moggi, M.F. Manfrin, F. Bolletta, M. Gleria, Solar energy conversion by water photodissociation, Science (80- 189 (1975) 852–856, https://doi.org/10.1126/science.189.4206.852.
[4] B. You, G. Han, Y. Sun, Electrocatalytic and photocatalytic hydrogen evolution integrated with organic oxidation, Chem. Commun. 54 (2018) 5943–5955, https://doi.org/10.1039/c8cc01830h.
[5] P. Zhang, Y. Liu, B. Tian, Y. Luo, J. Zhang, Synthesis of core-shell structured CdS@CeO2 and CdS@TiO2 composites and comparison of their photocatalytic activities for the selective oxidation of benzyl alcohol to benzaldehyde, Catal. Today 281 (2017) 181–188, https://doi.org/10.1016/j.cattod.2016.05.042.
[6] A. Badalyan, S.S. Stahl, Cooperative electrocatalytic alcohol oxidation with electron-proton-transfer mediators, Nature 535 (2016) 406–410, https://doi.org/10.1038/nature18008.
[7] H. Tateno, Y. Miseki, K. Sayama, Photoelectrochemical oxidation of benzylic alcohol derivatives on BiVO 4/WO 3 under visible light irradiation, ChemElectroChem (2017) 0–6, https://doi.org/10.1002/celc.201700710.
[8] L.M. Zhao, Q.Y. Meng, X.B. Fan, C. Ye, X.B. Li, B. Chen, V. Ramamurthy, C.H. Tung, L.Z. Wu, Photocatalysis with quantum dots and visible light: selective and efficient oxidation of alcohols to carbonyl compounds through a radical relay process in water, Angew. Chem. Int. Ed. 56 (2017) 3020–3024, https://doi.org/10.1002/anie.201700243.
[9] S. Marinković, N. Hoffmann, Efficient radical addition of tertiary amines to electron-def cient alkenes using semiconductors as photochemical sensitisers, Chem. Commun. 78 (2001) 1576–1578, https://doi.org/10.1039/b104387k.
[10] T. Morofuji, A. Shimizu, J. Yoshida, Electrochemical C–H amination: synthesis of aromatic primary amines via N -arylpyridinium ions, J. Am. Chem. Soc. 135 (2013) 5000–5003, https://doi.org/10.1021/ja402083e.
[11] L. Schulz, M. Enders, B. Elsler, D. Schollmeyer, K.M. Dyballa, R. Franke, S.R. Waldvogel, Reagent- and metal-free anodic C–C cross-coupling of aniline derivatives, Angew. Chem. Int. Ed. 56 (2017) 4877–4881, https://doi.org/10.1002/anie.201612613.
[12] R. Hayashi, A. Shimizu, J.I. Yoshida, The stabilized cation pool method: metal- and oxidant-free benzylic C-H/aromatic C-H cross-coupling, J. Am. Chem. Soc. 138 (2016) 8400–8403, https://doi.org/10.1021/jacs.6b05273.
[13] S. Lips, A. Wiebe, B. Elsler, D. Schollmeyer, K.M. Dyballa, R. Franke, S.R. Waldvogel, Synthesis of meta-Terphenyl-2,2″-diols by anodic C–C cross-coupling reactions, Angew. Chem. Int. Ed. 55 (2016) 10872–10876, https://doi.org/10.1002/anie.201605865.
[14] G. Han, Y.H. Jin, R.A. Burgess, N.E. Dickenson, X.M. Cao, Y. Sun, Visible-light-driven valorization of biomass intermediates integrated with H2Production catalyzed by ultrathin Ni/CdS nanosheets, J. Am. Chem. Soc. 139 (2017) 15584–15587, https://doi.org/10.1021/jacs.7b08657.
[15] N.A. Romero, D.A. Nicewicz, Organic photoredox catalysis, Chem. Rev. 116 (2016) 10075–10166, https://doi.org/10.1021/acs.chemrev.6b00057.
[16] J.M.R. Narayanam, C.R.J. Stephenson, Visible light photoredox catalysis: applications in organic synthesis, Chem. Soc. Rev. 40 (2011) 102–113, https://doi.org/10.1039/B913880N.
[17] K. Sivula, R. van de Krol, Semiconducting materials for photoelectrochemical energy conversion, Nat. Rev. Mater. 1 (2016) 15010, https://doi.org/10.1038/natrevmats.2015.10.
[18] J.Z. Bloh, R. Marschall, Heterogeneous photoredox catalysis: reactions, materials, and reaction engineering, Eur. J. Org. Chem. 2017 (2017) 2085–2094, https://doi.org/10.1002/ejoc.201601591.
[19] X. Lang, X. Chen, J. Zhao, Heterogeneous visible light photocatalysis for selective organic transformations, Chem. Soc. Rev. 43 (2014) 473–486, https://doi.org/10.1039/C3CS60188A.
[20] U.I. Gaya, A.H. Abdullah, Heterogeneous photocatalytic degradation of organic contaminants over titanium dioxide: a review of fundamentals, progress and problems, J. Photochem. Photobiol. C Photochem. Rev. 9 (2008) 1–12, https://doi.org/10.1016/j.jphotochemrev.2007.12.003.
[21] Y. Zhang, Y.J. Xu, Bi2WO6: a highly chemoselective visible light photocatalyst toward aerobic oxidation of benzylic alcohols in water, RSC Adv. 4 (2014) 2904–2910, https://doi.org/10.1039/c3ra46383d.
[22] S. Füldner, P. Pohla, H. Bartling, S. Dankesreiter, R. Stadler, M. Gruber, A. Pf tzner, B. König, Selective photocatalytic reductions of nitrobenzene derivatives using PbBiO2X and blue light, Green Chem. 13 (2011) 640–643, https://doi.org/10.1039/c0gc00857e.
[23] A. Savateev, I. Ghosh, B. König, M. Antonietti, Photoredox catalytic organic transformations using heterogeneous carbon nitrides, Angew. Chem. Int. Ed. 57 (2018) 2–14, https://doi.org/10.1002/anie.201802472.
[24] Y. Wang, X. Wang, M. Antonietti, Polymeric graphitic carbon nitride as a heterogeneous organocatalyst: from photochemistry to multipurpose catalysis to sustainable chemistry, Angew. Chem. Int. Ed. 51 (2012) 68–89, https://doi.org/10.1002/anie.201101182.
[25] Y. Zheng, J. Liu, J. Liang, M. Jaroniec, S.Z. Qiao, Graphitic carbon nitride materials: controllable synthesis and applications in fuel cells and photocatalysis, Energy Environ. Sci. 5 (2012) 6717–6731, https://doi.org/10.1039/c2ee03479d.
[26] G. Liu, Z. Ling, Y. Wang, H. Zhao, Near-infrared CdSexTe1-x@CdS "giant" quantum dots for efficient photoelectrochemical hydrogen generation, Int. J. Hydrogen Energy 43 (2018) 22064–22074, https://doi.org/10.1016/j.ijhydene.2018.10.076.
[27] X. Tong, X.T. Kong, C. Wang, Y. Zhou, F. Navarro-Pardo, D. Barba, D. Ma, S. Sun, A.O. Govorov, H. Zhao, Z.M. Wang, F. Rosei, Optoelectronic properties in near-infrared colloidal heterostructured pyramidal "giant" core/shell quantum dots, Adv. Sci. 5 (2018), https://doi.org/10.1002/advs.201800656.
[28] T. Simon, N. Bouchonville, M.J. Berr, A. Vaneski, A. Adrovic, D. Volbers, R. Wyrwich, M. Döblinger, A.S. Susha, A.L. Rogach, F. Jäckel, J.K. Stolarczyk, J. Feldmann, Redox shuttle mechanism enhances photocatalytic H2 generation on ni-decorated CdS nanorods, Nat. Mater. 13 (2014) 1–6, https://doi.org/10.1038/NMAT4049.
[29] K.L. Hardee, A.J. Bard, Semiconductor electrodes: V. The application of chemically vapor deposited iron oxide f lms to photosensitized electrolysis, J. Electrochem. Soc. 123 (1976) 1024–1026, https://doi.org/10.1149/1.2132984.
[30] K. Sivula, F. Le Formal, M. Grätzel, Solar water splitting: progress using hematite (α-Fe 2O3) photoelectrodes, ChemSusChem 4 (2011) 432–449, https://doi.org/10.1002/cssc.201000416.
[31] C. Li, Z. Luo, T. Wang, J. Gong, Surface, bulk, and interface: rational design of hematite architecture toward efficient photo-electrochemical water splitting, Adv. Mater. 30 (2018) 1–23, https://doi.org/10.1002/adma.201707502.
[32] R. Milan, S. Cattarin, N. Comisso, C. Baratto, K. Kaunisto, N.V. Tkachenko, I. Concina, Compact hematite buffer layer as a promoter of nanorod photoanode performances, Sci. Rep. 6 (2016) 1–10, https://doi.org/10.1038/srep35049.
[33] I.S. Cho, H.S. Han, M. Logar, J. Park, X. Zheng, Enhancing low-bias performance of hematite photoanodes for solar water splitting by simultaneous reduction of bulk, interface, and surface recombination pathways, Adv. Energy Mater. 6 (2016) 1–9, https://doi.org/10.1002/aenm.201501840.
[34] I. Cesar, K. Sivula, A. Kay, R. Zboril, M. Grätzel, Inf uence of feature size, f lm thickness, and silicon doping on the performance of nanostructured hematite photoanodes for solar water splitting, J. Phys. Chem. C 113 (2009) 772–782,

https://doi.org/10.1021/jp809060p.
[35] Y. Wu, W. Guo, M. Mishra, Y. Huang, J. Chang, T. Lee, Combinatorial studies on wet-chemical synthesized Ti-doped α-Fe 2 O 3 : how does Ti 4+ improve photoelectrochemical activity? ACS Appl. Nano Mater. 1 (2018) 3145–3154, https://doi.org/10.1021/acsanm.8b00316.
[36] Y. Ling, G. Wang, D.A. Wheeler, J.Z. Zhang, Y. Li, Sn-doped hematite nanostructures for photoelectrochemical water splitting, Nano Lett. 11 (2011) 2119–2125, https://doi.org/10.1021/nl200708y.
[37] M. Li, Y. Yang, Y. Ling, W. Qiu, F. Wang, T. Liu, Y. Song, X. Liu, P. Fang, Y. Tong, Y. Li, Morphology and doping engineering of Sn-doped hematite nanowire photoanodes, Nano Lett. 17 (2017) 2490–2495, https://doi.org/10.1021/acs.nanolett.7b00184.
[38] J.Y. Kim, J.W. Jang, D.H. Youn, G. Magesh, J.S. Lee, A stable and efficient hematite photoanode in a neutral electrolyte for solar water splitting: towards stability engineering, Adv. Energy Mater. 4 (2014) 1–7, https://doi.org/10.1002/aenm.201400476.
[39] G. Wang, Y. Ling, D.A. Wheeler, K.E.N. George, K. Horsley, C. Heske, J.Z. Zhang, Y. Li, Facile synthesis of highly photoactive α-Fe2O3-based f lms for water oxidation, Nano Lett. 11 (2011) 3503–3509, https://doi.org/10.1021/nl202316j.
[40] C. Miao, T. Shi, G. Xu, S. Ji, C. Ye, Photocurrent enhancement for Ti-doped Fe2O3thin f lm photoanodes by an in situ solid-state reaction method, ACS Appl. Mater. Interfaces 5 (2013) 1310–1316, https://doi.org/10.1021/am302575p.
[41] N.T. Hahn, C.B. Mullins, Photoelectrochemical performance of nanostructured Ti- and Sn-doped α-Fe2O3 photoanodes, Chem. Mater. 22 (2010) 6474–6482, https://doi.org/10.1021/cm1026078.
[42] D. Monllor-Satoca, M. Bärtsch, C. Fàbrega, A. Genç, S. Reinhard, T. Andreu, J. Arbiol, M. Niederberger, J.R. Morante, What do you do, titanium? Insight into the role of titanium oxide as a water oxidation promoter in hematite-based photoanodes, Energy Environ. Sci. 8 (2015) 3242–3254, https://doi.org/10.1039/c5ee01679g.
[43] O. Zandi, B.M. Klahr, T.W. Hamann, Highly photoactive Ti-doped ??-Fe_2O_3 thin f lm electrodes: resurrection of the dead layer, Energy Environ. Sci. 6 (2013) 634–642, https://doi.org/10.1039/c2ee23620f.
[44] D.M. Schultz, T.P. Yoon, Solar synthesis: prospects in visible light photocatalysis, Science 343 (80) (2014) 1239176, https://doi.org/10.1126/science.1239176.
[45] C.A. Mesa, A. Kaf zas, L. Francàs, S.R. Pendlebury, E. Pastor, Y. Ma, F. Le Formal, M.T. Mayer, M. Grätzel, J.R. Durrant, Kinetics of photoelectrochemical oxidation of methanol on hematite photoanodes, J. Am. Chem. Soc. 139 (2017) 11537–11543, https://doi.org/10.1021/jacs.7b05184.
[46] J.-R. Wang, Y. Fu, B.-B. Zhang, X. Cui, L. Liu, Q.-X. Guo, Palladium-catalyzed aerobic oxidation of amines, Tetrahedron Lett. 47 (2006) 8293–8297, https://doi.org/10.1016/j.tetlet.2006.09.088.
[47] C.M. Opriș, O.D. Pavel, A. Moragues, J. El Haskourib, D. Beltrán, P. Amorós, M.D. Marcos, L.E. Stof ea, V.I. Parvulescu, New multicomponent catalysts for the selective aerobic oxidative condensation of benzylamine to N-benzylidenebenzylamine, Catal. Sci. Technol. 4 (2014) 4340–4355, https://doi.org/10.1039/c4cy00795f.
[48] X. Zhao, J. Feng, N. Wang, X. Yao, W. Chen, S. Chen, Z. Huang, Z. Chen, The inf uence of Ti doping on morphology and photoelectrochemical properties of hematite grown from aqueous solution for water splitting, Energy Technol. 6 (2018) 2188–2199, https://doi.org/10.1002/ente.201800286.
[49] A. Annamalai, P.S. Shinde, T.H. Jeon, H.H. Lee, H.G. Kim, W. Choi, J.S. Jang, Fabrication of superior α-Fe2O3nanorod photoanodes through ex-situ Sn-doping for solar water splitting -Si, Sol. Energy Mater. Sol. Cells 144 (2016) 247–255, https://doi.org/10.1016/j.solmat.2015.09.016.
[50] Y. Zeng, Y. Han, Y. Zhao, Y. Zeng, M. Yu, Y. Liu, H. Tang, Y. Tong, X. Lu, Advanced Ti-doped Fe 2 O 3 @PEDOT core/shell anode for high-energy asymmetric supercapacitors, Adv. Energy Mater. 5 (2015) 1402176, https://doi.org/10.1002/aenm.201402176.
[51] D. Wang, H. Chen, G. Chang, X. Lin, Y. Zhang, A. Aldalbahi, C. Peng, J. Wang, C. Fan, Uniform doping of titanium in hematite nanorods for efficient photoelectrochemical water splitting, ACS Appl. Mater. Interfaces 7 (2015) 14072–14078, https://doi.org/10.1021/acsami.5b03298.
[52] Z. Fu, T. Jiang, L. Zhang, B. Liu, D. Wang, L. Wang, T. Xie, Surface treatment with Al 3+ on a Ti-doped α-Fe 2 O 3 nanorod array photoanode for efficient photoelectrochemical water splitting, J. Mater. Chem. A. 2 (2014) 13705, https://doi.org/10.1039/C4TA02527J.
[53] R. Franking, L. Li, M.A. Lukowski, F. Meng, Y. Tan, R.J. Hamers, S. Jin, Facile post-growth doping of nanostructured hematite photoanodes for enhanced photoelectrochemical water oxidation, Energy Environ. Sci. 6 (2013) 500–512, https://doi.org/10.1039/c2ee23837c.
[54] X. Chen, L. Liu, P.Y. Yu, S.S. Mao, Increasing solar absorption for photocatalysis with black hydrogenated titanium dioxide nanocrystals, Science 331 (80) (2011) 746–750, https://doi.org/10.1126/science.1200448.
[55] X. Lang, H. Ji, C. Chen, W. Ma, J. Zhao, Selective formation of imines by aerobic photocatalytic oxidation of amines on TiO2, Angew. Chem. Int. Ed. 50 (2011) 3934–3937, https://doi.org/10.1002/anie.201007056.
[56] Y. Zhang, L. Pei, Z. Zheng, Y. Yuan, T. Xie, J. Yang, S. Chen, J. Wang, E.R. Waclawik, H. Zhu, Heterojunctions between amorphous and crystalline niobium oxide with enhanced photoactivity for selective aerobic oxidation of benzylamine to imine under visible light, J. Mater. Chem. A. 3 (2015) 18045–18052, https://doi.org/10.1039/c5ta03214h.
[57] J.L. Dimeglio, B.M. Bartlett, Interplay of corrosion and photocatalysis during non-aqueous benzylamine oxidation on cadmium sulf de, Chem. Mater. 29 (2017) 7579–7586, https://doi.org/10.1021/acs.chemmater.7b02899.
[58] C.G. Zoski, Handbook of electrochemistry (2007), https://doi.org/10.1016/B978-0-444-51958-0.X5000-9.
[59] J. Zhang, R. García-Rodríguez, P. Cameron, S. Eslava, Role of cobalt–iron (oxy) hydroxide (CoFeO x) as oxygen evolution catalyst on hematite photoanodes, Energy Environ. Sci. 11 (2018) 2972–2984, https://doi.org/10.1039/C8EE01346B.
[60] C.C.L. McCrory, S. Jung, J.C. Peters, T.F. Jaramillo, Benchmarking heterogeneous electrocatalysts for the oxygen evolution reaction, J. Am. Chem. Soc. 135 (2013) 16977–16987, https://doi.org/10.1021/ja407115p.
[61] B. Hirschorn, M.E. Orazem, B. Tribollet, V. Vivier, I. Frateur, M. Musiani, Determination of effective capacitance and f lm thickness from constant-phase-element parameters, Electrochim. Acta 55 (2010) 6218–6227, https://doi.org/10.1016/j.electacta.2009.10.065.
[62] I. Mora-Seró, F. Fabregat-Santiago, B. Denier, J. Bisquert, R. Tena-Zaera, J. Elias, C. Lévy-Clément, Determination of carrier density of ZnO nanowires by electrochemical techniques, Appl. Phys. Lett. 89 (2006) 1–4, https://doi.org/10.1063/1.2390667.
[63] Z. Fu, T. Jiang, Z. Liu, D. Wang, L. Wang, T. Xie, Highly photoactive Ti-doped α-Fe2O3nanorod arrays photoanode prepared by a hydrothermal method for photoelectrochemical water splitting, Electrochim. Acta 129 (2014) 358–363, https://doi.org/10.1016/j.electacta.2014.02.132.
[64] B. Klahr, S. Gimenez, F. Fabregat-Santiago, T. Hamann, J. Bisquert, Water oxidation at hematite photoelectrodes: the role of surface states, J. Am. Chem. Soc. 134 (2012) 4294–4302, https://doi.org/10.1021/ja210755h.
[65] O. Savadogo, Correlation between the f at band potential of semiconductors and solvent donor numbers, Mater. Res. Bull. 23 (1988) 1451–1458, https://doi.org/10.1016/0025-5408(88)90271-1.
[66] C. Lohaus, A. Klein, W. Jaegermann, Limitation of Fermi level shifts by polaron defect states in hematite photoelectrodes, Nat. Commun. 9 (2018) 4309, https://doi.org/10.1038/s41467-018-06838-2.
[67] A. Shavorskiy, X. Ye, O. Karslloğlu, A.D. Poletayev, M. Hartl, I. Zegkinoglou, L. Trotochaud, S. Nemšák, C.M. Schneider, E.J. Crumlin, S. Axnanda, Z. Liu, P.N. Ross, W. Chueh, H. Bluhm, Direct mapping of band positions in doped and undoped hematite during photoelectrochemical water splitting, J. Phys. Chem. Lett. 8 (2017) 5579–5586, https://doi.org/10.1021/acs.jpclett.7b02548.
[68] I. Zonno, A. Martinez-Otero, J.C. Hebig, T. Kirchartz, Understanding Mott-Schottky measurements under illumination in organic bulk heterojunction solar cells, Phys. Rev. Appl. 7 (2017) 1–8, https://doi.org/10.1103/PhysRevApplied.7.034018.
[69] N. Dalle Carbonare, S. Carli, R. Argazzi, M. Orlandi, N. Bazzanella, A. Miotello, S. Caramori, C.A. Bignozzi, Improvement of the electron collection efficiency in porous hematite using a thin iron oxide underlayer: towards efficient all-iron based photoelectrodes, Phys. Chem. Chem. Phys. 17 (2015) 29661–29670, https://doi.org/10.1039/c5cp04152j.

Raffaello Mazzaro received his PhD in Chemistry in 2016, in collaboration between the CNR- IMM institute in Bologna and the chemistry department G. Ciamician of the University of Bologna, Italy. He is currently a Kempe and Knut & Alice Wallenberg postdoctoral fellow at Luleå University of Technology, Sweden. His interests and past activities are mainly focused on energy conversion processes performed by optically active nanomaterials, such as quantum dots and metal oxides nanostructures.

Sara Boscolo Bibi graduated at Ca Foscari University of Venice (Italy) in 2018. She did her master thesis in the Department of Engineering Sciences and Mathematics, under the supervision of Dr. Raffaello Mazzaro and Prof. Dr. Vomiero at Luleå University of Technology (Sweden), working on nanostructured hematite photoelectrodes for photoelectrochemical organic reactions and all-oxide solar cells. Currently, she is a Ph.D. candidate at Stockholm University and joined the group Ultrafast Laser Spectroscopy & Matter Interaction of Prof. Dr. Tony Hansson. Her major interest is the investigation of microscopic processes that govern heterogeneous catalysis involved in the carbon dioxide reduction using vibrational sum-frequency generation (VSFG) spectroscopy.

Mirco Natali is assistant professor at the Department of Chemical and Pharmaceutical Sciences of the University of Ferrara. From the same institution he received his PhD in Chemical Sciences in 2014 working in the group of Prof. Franco Scandola. His research interests embrace several aspects of artif cial photosynthesis as well as fundamental studies on photoinduced energy and electron transfer processes.

Giacomo Bergamini obtained his PhD in Chemical Science at the University of Bologna in 2007 under the supervision of Prof. Vincenzo Balzani. He currently an Associate Professor at the University of Bologna, and is co-author of more than 90 scientif c papers in refereed international journals. He is the Coordinator of the H2020-MSCA-ITN-2016 PHOTOTRAIN

Vittorio Morandi, Ph.D. is Deputy Director of the Unit of Bologna of the CNR-IMM Institute (http://www.bo.imm.cnr.it), chair and member of committees of several international conferences, and permanent reviewer of international projects and top-level scientif c journals. He is directly involved in several national and international research projects and industrial contracts, and has published more than 120 papers (H = 28) on international peer-reviewed journals. His main research interests concern the development of advanced electron microscopy techniques, their application to the study nanomaterials, and the synthesis, characterization, and technological integration of graphene and graphene-based materials.

Paola Ceroni is full professor at the University of Bologna. In 1998 she obtained her PhD degree in Chemical Sciences at the University of Bologna, after a period in the United States (Prof. Allen J. Bard's laboratory). Current research is focused on photochemistry and electrochemistry of supramolecular systems and nanocrystals. Her research on luminescent silicon nanocrystals was funded by an ERC Starting Grant *PhotoSi* and an ERC Proof of Concept *SiNBiosys*. She is fellow of the Royal Society of Chemistry and Associate Editor of Dalton Transactions. She is co-author of 190 scientif c papers and of a book on photochemistry (Wiley-VCH, 2014).

Alberto Vomiero is a professor in Experimental Physics at the Department of Engineering Sciences and Mathematics, Luleå University of Technology (LTU), Sweden and a professor in Industrial Engineering at the Department of Molecular Sciences and Nanosystems, Ca Foscari University of Venice, Italy. His main interests are in the synthesis of composite nanomaterials for environmental applications, including solar cells, water splitting and photocatalysis. He has published more than 160 scientif c papers in peer reviewed Journals. He is a former Marie Curie International Outgoing Fellow of the European Commission, Fellow of the Swedish Foundations, of the Royal Society of Chemistry (UK), and of several other Societies.